



Insect recognition based on integrated region matching and dual tree complex wavelet transform*

Le-qing ZHU¹, Zhen ZHANG^{†‡2}

¹College of Computer Science and Information Engineering, Zhejiang Gongshang University, Hangzhou 310018, China)

²Key Lab of Forest Protection of State Forestry Administration, Research Institute of Forest Ecology, Environment and Protection, Chinese Academy of Forestry, Beijing 100091, China)

[†]E-mail: zhangzhen@caf.ac.cn

Received Dec. 4, 2009; Revision accepted Mar. 31, 2010; Crosschecked Nov. 4, 2010

Abstract: To provide pest technicians with a convenient way to recognize insects, a novel method is proposed to classify insect images by integrated region matching (IRM) and dual tree complex wavelet transform (DTCWT). The wing image of the lepidopteran insect is preprocessed to obtain the region of interest (ROI) whose position is then calibrated. The ROI is first segmented with the *k*-means algorithm into regions according to the color features, properties of all the segmented regions being used as a coarse level feature. The color image is then converted to a grayscale image, where DTCWT features are extracted as a fine level feature. The IRM scheme is undertaken to find *K* nearest neighbors (KNNs), out of which the nearest neighbor is searched by computing the Canberra distance of DTCWT features. The method was tested with a database including 100 lepidopteran insect species from 18 families and the recognition accuracy was 84.47%. For the forewing subset, a recognition accuracy of 92.38% was achieved. The results showed that the proposed method can effectively solve the problem of automatic species identification of lepidopteran specimens.

Key words: Lepidopteran insects, Auto-classification, *k*-means algorithm, Integrated region matching (IRM), Dual tree complex wavelet transform (DTCWT)

doi:10.1631/jzus.C0910740

Document code: A

CLC number: TP391.41

1 Introduction

Insect recognition is the basis of crop pest and disease control in agriculture and forestry. Traditionally, experts observe the external features of insects and then compare these features with specimens, which is time consuming and labor exhausting. Using computer technologies, such as image processing and pattern recognition, can be a more accurate and efficient way to achieve insect auto-classification than the traditional method. An insect image contains abundant information which plain text is unable to offer. The wing shape, color, and texture patterns of

lepidopteran insects are species-specific, and can be used taxonomically.

Several attempts have been made to build automatic insect identification systems based on image analysis (Batra, 1988; Yu *et al.*, 1992; Roth *et al.*, 1999; Weeks *et al.*, 1999; Schroder *et al.*, 2002). These systems differ in their level of automation. Some of them require pointing to wing landmarks with a mouse (e.g., Schroder *et al.*, 2002), and others require interventions at various stages of largely automatic processes (e.g., Yu *et al.*, 1992). The wing positioning has proven to be time consuming and this was considered by Weeks *et al.* (1999) as the main limitation of their system. Tofilski (2004) developed a program named DrawWing, which can be used to extract landmarks from an insect wing automatically and discriminate between males of *Dolichovespula sylvestris* and *Dolichovespula saxonica*. Mayo and

[‡] Corresponding author

^{*} Project (No. 2006AA10Z211) supported by the National High-Tech Research and Development Program (863) of China

© Zhejiang University and Springer-Verlag Berlin Heidelberg 2011

Watson (2007) adopted data mining techniques for automatic species identification, and a collection consisting of the images of 774 live moth individuals (35 species) was used for testing. Using the machine learning toolkit WEKA to classify the moths, they achieved a greater level of accuracy (85%) using support vector machines (SVMs) without any manual specification of a region of interest (ROI). MacLeod (2007) systematically introduced theories and approaches in automated taxon identification, and described three main image-based systems in detail: the digital automated identification system (DAISY) (Watson *et al.*, 2003; Gaston and O'Neill, 2004), the species identification automated system (SPIDA) (Russell *et al.*, 2007), and the automated bee identification system (ABIS) (Arbuckle *et al.*, 2001). The former two use a neural network for the core classification task. DAISY is a generic pattern matching system (Weeks *et al.*, 1999) initially developed at the Natural History Museum in London (BMNH) under the aegis of the Biotechnology and Biological Sciences Research Council (BBSRC) and UK Government Darwin Initiative funding. DAISY has in the past been used for classifying fish, pollen, and plants of different types, although the main focus appears to be moths. SPIDA, on the other hand, was specifically designed to distinguish between 121 species of Australian spider; recently it has also been tested on bumblebee wings with limited success. ABIS was first developed by Arbuckle *et al.* (2001) in the University of Bonn, and it is a specialist pattern recognition system suitable only for insects with membranous wings.

Our computer-based recognition approach is motivated by the considerable progress made recently in content-based image retrieval (CBIR). A region-based retrieval system applies image segmentation (Shi and Malik, 2000; Wang *et al.*, 2001a) to decompose an image into regions. For lepidopteran insects, their wings are often covered by colorful regions or splashes. The color, position, and shape of splashes are very unique and can be used as basis for species discrimination. The k -means algorithm is used to cluster the feature vectors into several classes with each class corresponding to one region in the segmented image. The integrated region matching (IRM) (Wang *et al.*, 2001b) measures the overall similarity between images by integrating properties of all the regions in the images. The approximate shift

invariant property of the dual tree complex wavelet transform (DTCWT) and its good directional selectivity in 2D make it a very appealing choice for insect image recognition. DTCWT features are extracted from grayscale images, used as texture features for fine matching. The K nearest neighbors (KNNs) resulting from IRM participate in DTCWT matching to find the nearest neighbor as the finally matched species.

2 Image acquisition and preprocessing

2.1 Image acquisition

One hundred species with relatively good image quality are selected as the insect species of interest in this research; two to six adult specimens for each species are prepared (see the Appendix). The image acquisition system is composed of an image acquisition platform which provides stable illumination and a color digital camera (Nikon D200, with 43 mm zoomable lens) for taking pictures of insects from the upside of the platform. Two fluorescent lamps provide the platform's light source. Digital images taken by the camera are transferred to the computer. A set of images is acquired and saved. All the image samples are captured from the right wing of the insect. Some are forewing together with hinder wing; the rest only forewing. Fig. 1 shows some of the acquired insect image samples.

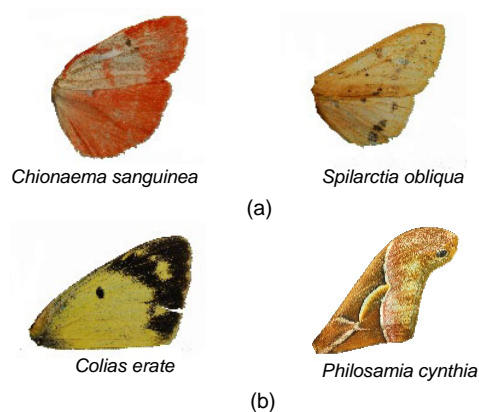


Fig. 1 Acquired insect wing images
(a) Forewing together with hinder wing; (b) Forewing

2.2 Image preprocessing

The captured image is resized to a smaller one (248×200 pixels), maintaining the original aspect ratio, so as to make the computation of IRM and

DTCWT tractable while the accuracy is also maintained. The resized image is first filtered with a mean shift algorithm (Comaniciu and Meer, 2002) (Fig. 2b), then converted to grayscale space (Fig. 2c), and binarized with a certain threshold (Fig. 2d). The foreground region then can be segmented out from the background by finding the region inside the maximum contour. To diminish the effect of rotation and translation variation during image acquisition, a standard coordinate system must be located. We first find the centroid of the foreground region and the leftmost point on the contour, and then connect them and rotate the image around the centroid until the connected line is horizontal (Fig. 2e). This is not accurate enough for eliminating rotation and translation variations. In general, the up edge and down edge of the insect wing are stable and can be used for standardizing the wing position. We track on the

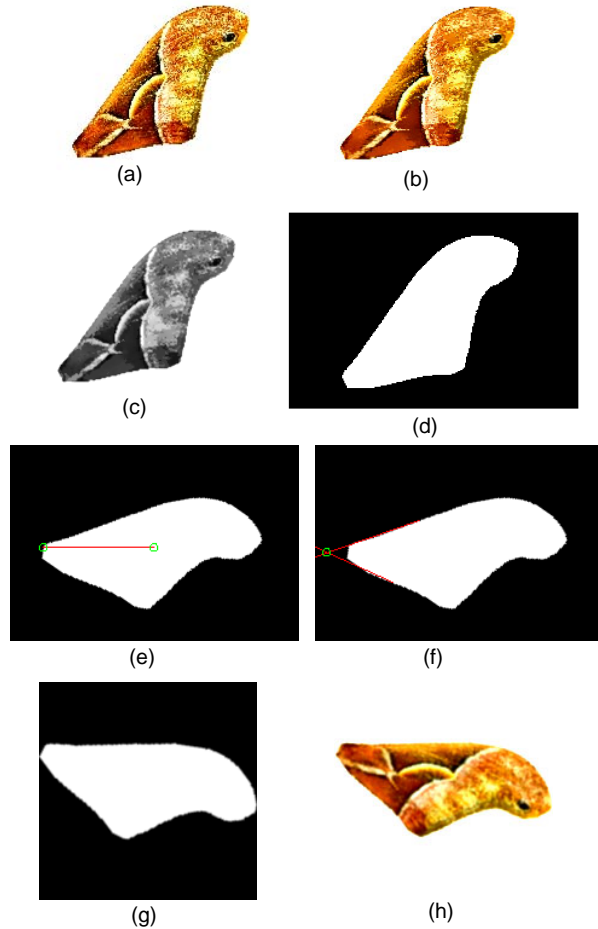


Fig. 2 Intermediate results of the image preprocessing
 (a) Original image; (b) Mean shift filtered; (c) Transform to grayscale; (d) Binarized; (e) Initial rotation; (f) Fitting edges; (g) Region of interest; (h) Aligned color image

contour of the wing, and use the least-squares method to fit the up edge and down edge with straight lines. Assuming that the up edge starts at the upmost point and ends at the leftmost point on the contour, we obtain the point set $P_0 = \{(x_i^0, y_i^0) | i = 0, 1, \dots, n_0\}$ between the start and the end on the contour; assuming that the down edge starts at the leftmost point and ends at the downmost point on the contour (the initial rotation mentioned above is to assure the downmost point to be the end of the down edge), we obtain another point set $P_1 = \{(x_i^1, y_i^1) | i = 0, 1, \dots, n_1\}$. The up edge and down edge can be fitted as

$$y = k_j x + b_j, \quad (1)$$

$$k_j = \frac{\sum_{i=1}^{n_j} x_i^j \sum_{i=1}^{n_j} y_i^j - n_j \sum_{i=1}^{n_j} x_i^j y_i^j}{\left(\sum_{i=1}^{n_j} x_i^j \right)^2 - n_j \sum_{i=1}^{n_j} (x_i^j)^2}, \quad (2)$$

$$b_j = \frac{1}{n_j} \left(\sum_{i=1}^{n_j} y_i^j - k_j \sum_{i=1}^{n_j} x_i^j \right), \quad (3)$$

where $j=0$ and 1 represent the up edge and down edge, respectively.

The position calibration is completed by rotating around the intersection of these two fitted lines (Fig. 2f) until the up edge is horizontal (Fig. 2g). The square area refined by the maximum bound-box (Fig. 2h) is considered afterward as ROI, which is normalized into size 128×128 pixels and is smoothed using the Gaussian kernel of aperture size 3×3 with the standard sigma before feature extraction (Zhu and Zhang, 2010).

3 Two-level feature extraction

3.1 Color feature extraction

The preprocessed image is segmented into regions based on the k -means algorithm using the color feature. Only the region inside the mask (Fig. 2g) is segmented. The segmentation accuracy of this system is not crucial because an IRM scheme is used to provide robustness against inaccurate segmentation. The k -means algorithm is used to cluster the feature vectors into several classes with each class corresponding

to one region in the segmented image. We use pixel-wise segmentation to classify pixels into regions according to their color properties.

Suppose observations are $\{x_i | i=1, 2, \dots, L\}$. The goal of the k -means algorithm is to partition the observations into k groups with means $\hat{x}_1, \hat{x}_2, \dots, \hat{x}_k$ such that

$$D(k) = \sum_{i=1}^L \min_{1 \leq j \leq k} (x_i - \hat{x}_j)^2 \quad (4)$$

is minimized. The k -means algorithm does not specify how many clusters to choose. We adaptively choose the number of clusters k by gradually increasing k and stopping when a criterion is met. We start with $k=2$ and stop increasing k if one of the following conditions is satisfied:

1. The distortion $D(k)$ is below a threshold. A low $D(k)$ indicates high purity in the clustering process. The threshold is not critical because the IRM measure is not sensitive to k .

2. The first derivative of distortion with respect to k , $D(k-1)-D(k)$, is below a threshold with comparison to the average derivative at $k=2, 3$. A low $D(k-1)-D(k)$ indicates convergence in the clustering process.

3. k exceeds an upper bound. We allow an image to be segmented into a maximum of 15 segments. That is, we assume that an image has less than 15 distinct splashes. Usually, the segmentation process generates a much smaller number of segments in an image. The threshold is rarely met.

Three features are used for segmentation, i.e., the three components of each pixel's color. We use the well-known RGB color space. Examples of segmentation results of different insects are shown in Fig. 3. Segmented regions are shown in their representative colors. After the segmentation is completed, the percentage and the centroid coordinates of the regions (which are all normalized to 0–1 range) are computed as the remaining three feature components.

3.2 DTCWT feature extraction

Recent studies show that people interpret an image in many different directions and frequency channels, which is similar to the multiple-resolution property of a wavelet. For this reason, wavelet transform has been widely applied to image

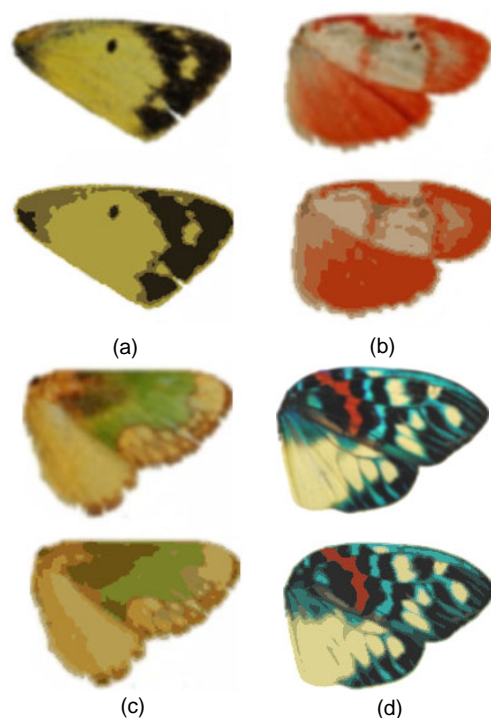


Fig. 3 Segmentation results using the k -means clustering algorithm

(a) *Colias erate*, $k=3$; (b) *Chionaema sanguinea*, $k=5$; (c) *Parasa pastoralis*, $k=7$; (d) *Erasmia pulchella chinensis*, $k=11$. In each subfigure, the top and bottom rows represent the original image and the segmented region, respectively

processing, as in texture analysis and texture synthesis. DTCWT has the advantages of approximate shift invariance, good directional selectivity, high computational efficiency, and low redundancy (Kokare *et al.*, 2005), and thus can be used to analyze insect wing image texture.

DTCWT, proposed by Kingsbury (2001), is performed based on a real wavelet transform instead of using complex coefficient filters. A signal is decomposed in terms of a complex shifted and dilated mother wavelet. DTCWT is implemented by using separable transforms and combining subband signals appropriately. Although non-separable, it inherits the computational efficiency of separable transforms.

DTCWT consists of two parallel wavelet trees constructed with traditional orthogonal wavelet filters. One is the odd length high-pass filter, where the sample sequence is even-symmetric with respect to the midpoint; the other is the even length high-pass filter, which is odd-symmetric with respect to the midpoint. They turn out to be the real part and

imaginary part of the complex wavelet after alternatively oddly and evenly filtered, respectively. The decomposed image results in six wavelet subbands on each level. Compared to the traditional wavelet, DTCWT can be easily reconstructed with its approximate shift invariance and good directional selectivity properties.

Specifically, the 1D DTCWT is implemented using two filter banks operating on the same data in parallel. It contains two parallel 1D discrete wavelet transform trees (trees A and B). Let $h_0(n)$, $h_1(n)$ and $g_0(n)$, $g_1(n)$ be the high- and low-pass filters of trees A and B, respectively. 1D DTCWT is as shown by equation $\psi(t)=\psi_h(t)+j\psi_g(t)$, where $\psi_h(t)$ and $\psi_g(t)$ are the wavelets corresponding to trees A and B, respectively.

2D DTCWT can be defined as $\psi(x, y)=\psi(x)\psi(y)$, where $\psi(x)$ and $\psi(y)$ are two wavelets:

$$\psi(x)=\psi_h(x)+j\psi_g(x), \quad (5)$$

$$\psi(y)=\psi_h(y)+j\psi_g(y), \quad (6)$$

where $\psi_h(\cdot)$ and $\psi_g(\cdot)$ are the high and low filter groups of the real wavelet transform, respectively. Specifically, $\psi_g(t)$ is approximately the Hilbert transform of $\psi_h(t)$:

$$\psi_g(t) \approx H\{\psi_h(t)\}. \quad (7)$$

The 2D discrete wavelet basis includes three directions: horizontal, vertical, and diagonal (Fig. 4a). The 2D DTCWT basis has six directions oriented at $\pm 15^\circ$, $\pm 45^\circ$, $\pm 75^\circ$ (Fig. 4b), which shows that 2D DTCWT has a better orientation selection property than 2D DWT. Since the image is decomposed into more abundant texture directions, 2D DTCWT can describe the texture feature better than 2D DWT.

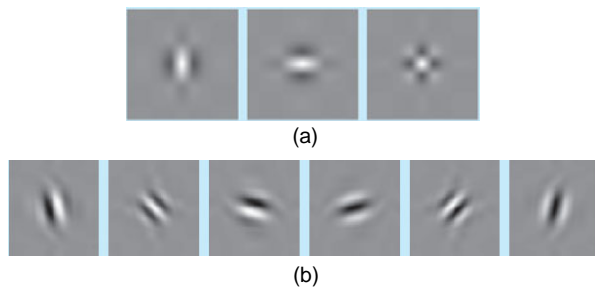


Fig. 4 Impulse responses of DWT (a) and DTCWT (b)

4 Hierarchical recognition

The matching of these two-level features can be organized with a hierarchical manner. First, the KNNs are searched with IRM; then the nearest neighbor (NN) is found with DTCWT texture features among previously searched KNNs.

4.1 Integrated region matching

Assume that images 1 and 2 are represented by region sets $R_1=\{r_1, r_2, \dots, r_m\}$ and $R_2=\{r'_1, r'_2, \dots, r'_n\}$, respectively, where r_i or r'_i is the descriptor of region i . Denote the distance between regions r_i and r'_j as $d(r_i, r'_j)$, written as $d_{i,j}$ in short. To compute the similarity measure between region sets R_1 and R_2 , $d(R_1, R_2)$, we first match all regions in the two images. To increase robustness against segmentation errors, a region is allowed to be matched to several regions in another image. A matching between r_i and r'_j is assigned with a significance credit $s_{i,j}$, $s_{i,j}>0$. The significance credit indicates the importance of the matching for determining similarity between images. The matrix

$$\mathbf{S} = \begin{bmatrix} s_{1,1} & s_{1,2} & \dots & s_{1,n} \\ s_{2,1} & s_{2,2} & \dots & s_{2,n} \\ \vdots & \vdots & & \vdots \\ s_{m,1} & s_{m,2} & \dots & s_{m,n} \end{bmatrix} \quad (8)$$

is referred to as the significance matrix. Then the distance between the two region sets is the summation of all the weighted edge lengths, i.e.,

$$d(R_1, R_2) = \sum_{i,j} s_{i,j} d_{i,j}, \quad (9)$$

which is called the IRM distance. The problem of defining the distance between two region sets is then converted to choosing the significance matrix \mathbf{S} . A natural issue to raise is what constraints should be put on $s_{i,j}$ so that the admissible matching yields a good similarity measure. Assuming that the significance of r_i in image 1 is p_i and the significance of r'_j in image 2 is p'_j , we require that:

$$\sum_{j=1}^n s_{i,j} = p_i, \quad i = 1, 2, \dots, m, \quad (10)$$

$$\sum_{i=1}^m s_{i,j} = p'_j, \quad j = 1, 2, \dots, n. \quad (11)$$

For normalization, we have $\sum_{i=1}^m p_i = 1$, $\sum_{j=1}^n p'_j = 1$. The fulfillment of significance ensures that all the regions play a role for measuring similarity. The IRM algorithm attempts to fulfill the significance credits of regions by assigning as much significance as possible to the region link with a minimum distance, which is called the most similar highest priority (MSHP) principle. Initially, assume $d_{i,j'}$ is the minimum distance. We set $s_{i,j'} = \min(p_i, p'_{j'})$. Without loss of generality, we assume $p_i \leq p'_{j'}$. Then $s_{i,j'} = 0$ for $j \neq j'$ since the link between regions i' and j' has filled the significance of region i' . The significance credit left for region j' is reduced to $p'_{j'} - p_i$. The updated matching problem is then turned into solving $s_{i,j}$, $i \neq i'$, by the MSHP rule, under constraints:

$$\sum_{j=1}^n s_{i,j} = p_i, \quad 1 \leq i \leq m, \quad i \neq i', \quad (12)$$

$$\sum_{i=1, i \neq i'}^m s_{i,j} = p'_j, \quad 1 \leq j \leq n, \quad j \neq j', \quad (13)$$

$$\sum_{i=1, i \neq i'}^m s_{i,j'} = p'_{j'} - p_i, \quad s_{i,j} \geq 0, \quad 1 \leq j \leq n. \quad (14)$$

We apply the previous procedure to the updated problem. The iteration stops when all the significance credits $s_{i,j}$ have been assigned. The algorithm is summarized as follows:

1. Set $L = \{ \}$, and denote $M = \{ (i, j) | i = 1, 2, \dots, m; j = 1, 2, \dots, n \}$.
2. Choose the minimum $d_{i,j}$ for $(i, j) \in M - L$. Label the corresponding (i, j) as (i', j') .
3. $\min(p_i, p'_{j'}) \rightarrow s_{i',j'}$.
4. If $p_i \leq p'_{j'}$, set $s_{i',j} = 0, j \neq j'$; otherwise, set $s_{i,j'} = 0, i \neq i'$.
5. $p_i - \min(p_i, p'_{j'}) \rightarrow p_i$.
6. $p'_{j'} - \min(p_i, p'_{j'}) \rightarrow p'_{j'}$.
7. $L + \{ (i', j') \} \rightarrow L$.
8. If $\sum_{i=1}^m p_i > 0$ and $\sum_{j=1}^n p'_j > 0$, go to step 2;

otherwise, stop.

4.2 Dual tree complex wavelet matching

If the image is separated into $M \times M$ blocks, each is transformed with DTCWT. We give each block a weight w_m according to its coverage by mask, i.e.,

$$w_m = \frac{s_m}{s_b}, \quad (15)$$

where s_b is the block size in area, and s_m is the area of the m th block covered by the mask.

Then the Canberra distance can be calculated with

$$\text{Dist}_2 = \sum_{m=1}^{M \times M} \frac{\sum_{l=1}^L \sum_{b=1}^B |\mathcal{M} - \mathcal{M}'| + \sum_{l=1}^L \sum_{b=1}^B |\mathcal{N} - \mathcal{N}'|}{\sum_{l=1}^L \sum_{b=1}^B |\mathcal{M} + \mathcal{M}'| + \sum_{l=1}^L \sum_{b=1}^B |\mathcal{N} + \mathcal{N}'|} \frac{s_i}{s_b}, \quad (16)$$

where

$$\begin{aligned} \mathcal{M} &= w_m \mu_m(l, b), \quad \mathcal{M}' = \hat{w}_m \hat{\mu}_m(l, b), \\ \mathcal{N} &= w_m \sigma_m(l, b), \quad \mathcal{N}' = \hat{w}_m \hat{\sigma}_m(l, b), \end{aligned}$$

$\mu_m(l, b)$ and $\hat{\mu}_m(l, b)$ represent the mean values of coefficients of the m th block, l th decomposition, and b -level frequency band from the testing image and template image respectively, and $\sigma_m(l, b)$ and $\hat{\sigma}_m(l, b)$ represent standard deviations of coefficients of the m th block, l -level decomposition, and b -level frequency band from the testing image and template image respectively. M represents the number of blocks that the image is segmented into along the vertical and horizontal directions. L represents the levels of DTCWT. B ($B=6$ in this study) represents the number of frequency bands that the blocks are decomposed into with DTCWT on each level.

There is a matching score for the final matched template, which is calculated as

$$\text{Score} = 1 - (0.3d_{\text{IRM}} + 0.7d_{\text{DTCWT}}), \quad (17)$$

where d_{IRM} is the IRM distance and d_{DTCWT} is the DTCWT distance. Only when the score is larger than the threshold (0.7), is the final match accepted. The score is a reference for acceptance confidence.

5 Experimental results

As mentioned in Section 2.1, 100 species were prepared for testing, with two to six adult specimens for each and 425 specimens in total (see the Appendix). All the images were collected from different specimens with the same platform. Although we tried our best to keep the wings of specimens widely open before taking pictures, there are still apparent variations in pose for specimens of some species (as shown later in Figs. 6a and 6b). Certain specimens have apparent debris and damage (Fig. 6c). Intra-species chromatism among individuals also exists (Fig. 6d). All the tests were run on an Intel Core2 2.16 GHz, 1 GB RAM PC, with Visual Studio 2005 and OpenCV on the Windows XP operating system as the software developing environment. Two-level features have been generated and are stored in the database. Every sample is matched with the rest of the specimens in the database in a hierarchical manner.

The distribution of inner- and inter-class IRM distances (Fig. 5a) showed that the inner-class distances concentrated around 0.15 and that the inter-class distances distributed around 0.3. The distance distribution of the DTCWT feature (Fig. 5b) showed that the inner-class distances concentrated around 0.2 and that the inter-class distances distributed in a wide range around 0.5. Features of both levels exhibited high convergence of inner-class similarities and good dispersion of inter-class discrimination.

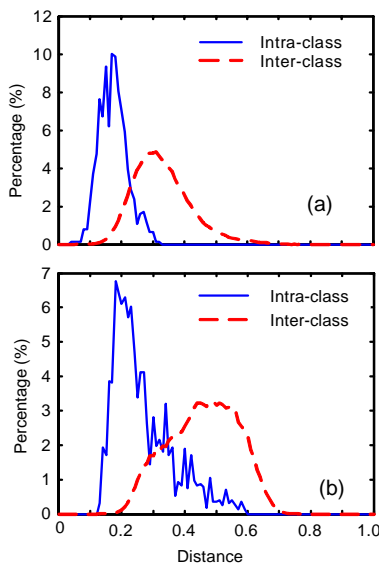


Fig. 5 Imposter and genuine distributions for level-1 and level-2 features

(a) Distribution of the IRM distance; (b) Distance distribution of DTCWT features

The optimal block size M and complex wavelet decomposition level L for the texture feature should be tested. The results are shown in Table 1 when $K=20$ (K is the number of IRM KNNs admissible to level-2 DTCWT matching), $M=1, 2, 4, 8, 16$ and $L=2, 3$. It is shown that the best performance was obtained when $M=8$ and $L=3$.

Table 1 Recognition rate with different numbers of image blocks (M) and wavelet decomposition levels (L)

M	Recognition rate (%)	
	$L=2$	$L=3$
1	66.12	66.12
2	72.94	76.47
4	81.18	81.18
8	83.06	83.75
16	80.24	—

$K=20$, K is the number of IRM KNNs admissible to level-2 DTCWT matching

The optimal number of KNNs was also tested. The insect recognition rates under $K=5, 10, 15, 20, 25, 30, 35, 40$ with hierarchical matching were shown in Table 2. It can be seen that the optimal recognition rate, 84.47%, was obtained under $K=30$.

Table 2 Recognition accuracy under different K values

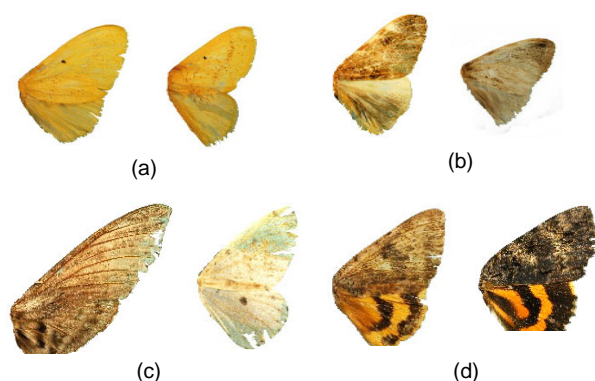
K	Recognition rate (%)	K	Recognition rate (%)
5	77.41	25	84.24
10	78.82	30	84.47
15	81.18	35	84.24
20	83.75	40	83.53

The recognition results under optimal K, M, L ($K=30, M=8, L=3$) are given in Table 3. There were totally 425 specimens in the database, and 425 rounds of identification have been performed. A total of 105 specimens (24 species) were shown in forewing images and the rest were forewing together with hinder wing. Finally, we obtained 359 correct answers, the recognition accuracy being 84.47%, while for the forewing images subset, the recognition rate was higher, 92.38%. The forewing images provided better results than the whole right wing images, because samples of whole wing images differed a lot in extent of forewing overlapping with hinder wing (Figs. 6a and 6b). We found that some species were often confused with each other during testing (Fig. 7), which brought down the recognition rate considerably. These confused pairs mostly belong to the same subject. To discriminate these pairs, more information (e.g., ventral images) is needed.

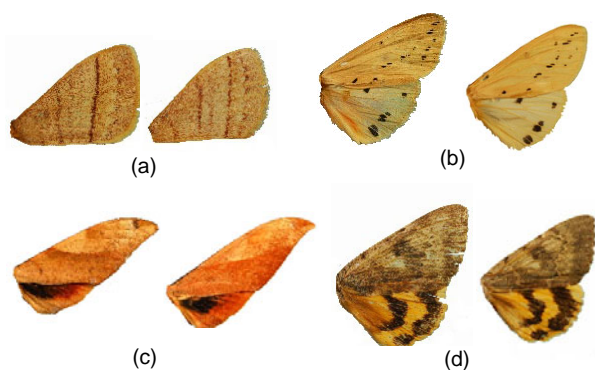
Table 3 Recognition results of insect auto-classification

Parameter	Value	
	Overall images	Forewing images
Number of searching rounds	425*	105**
Number of correct answers	359	97
Number of false answers	66	8
Recognition rate	84.47%	92.38%

* 100 species; ** 24 species

**Fig. 6 Samples from the same species with apparent difference on forewing overlapping hinder wing**

(a) Different samples of *Euproctis decussata*; (b) Different samples of *Pida postalba*; (c) Samples (*Herse convolvuli* and *Naxa seriaria*) with debris or damage; (d) Intra-species chromatism (*Ephesia ella*)

**Fig. 7 Similar samples from different species**

(a) *Eupterote lativittata* (left) and *Eupterote diffusa* (right); (b) *Spilarctia obliqua* (left) and *Spilarctia flavalis* (right); (c) *Clanis bilineata tsingtauca* (left) and *Clanis deucalion* (right); (d) *Ephesia ella* (left) and *Ephesia butleri* (right)

With 49 species classifiers, an identification accuracy of 86% was reported with DAISY (Weeks *et al.*, 1999), but the identification rate of DAISY declined with the increase of the number of species classifiers. The form of the relationship between the proportion of correct identifications and the number

of species classifiers implies that with 100 classifiers this rate would decline to below 80%. For SPIDA (Russell *et al.*, 2007), the accuracy of identification for well represented species (15–20 unique samples available for training) was consistently high—in the range of 90%–96%, with accuracy levels for under-represented groups (<10 unique specimens) being much lower, perhaps below 75%. There were only two to six unique specimens for each species in this study, which means that there were at most one to five samples available for training (the rest of the samples for testing). This small training dataset would make principal component analysis (PCA) or artificial neural networks (ANNs) inefficient. In the same sense, this small size of training set also makes SVM and the Gaussian mixture model (GMM) unavailable.

The time cost for feature extraction and matching (Table 4) showed that our insect recognition method can meet the requirement of real time applications. In the case that many thousands of classes have to be dealt with, insect images were first classified based on their semantics such as their genera or subject. Then the system can restrict the search to images with a particular semantic type to realize real time responses.

Table 4 Time cost for each processing step of the recognition algorithm

Processing step	Time (ms)
Preprocessing	80
Color feature extraction	47
DTCWT feature extraction	608
IRM	1.6
DTCWT matching	9.2
Average searching*	1103

* 425 samples

6 Conclusions

This paper deals with a novel insect recognition algorithm based on IRM and DTCWT, which can be used to identify insect species from low resolution wing images. The presented automatic identification system is accurate and efficient in recognizing specific species of insects. The algorithm is developed to recognize lepidopteran insects whose color and texture features are salient, while their venation features are difficult to extract because their surfaces are covered by colorful scales. The proposed method was

tested in a database including 100 species and the recognition accuracy is 84.47%. For the forewing subset, the recognition accuracy is even higher (92.38%). The relative position of forewing and hinder wing is variable, which affects the overall recognition rate of the whole wing images. Thus, we are preparing to establish a separate database for forewing images and hinder wing images. At present, the images analyzed were obtained using one camera, and color differences would be brought about if insect images were taken with a different camera. Although Wang *et al.* (2001b) showed that IRM is a robust method for image matching, its robustness was not evaluated with real data. In the future, we will collect more samples of insects with different cameras and further test the proposed method with those newly added datasets. The proposed method is tested on lepidopteran insects because most of lepidopteran insects have rich colorful splashes on their wings and the IRM approach can be employed. As for other classes of insects (e.g., flies and bees with membranous wings), the IRM approach might not be effective, but the DTCWT approach can still be employed. This will be another direction for our future research.

This paper applies CBIR technology to insect taxonomy research, and this technology is a good complement to traditional insect auto-classification based on venation features or mathematic morphology. The method can be a tool for insect auto-classification, which insect researchers can use as reference for insect taxonomy.

References

- Arbuckle, T., Schröder, S., Steinhage, V., Wittmann, D., 2001. Biodiversity Informatics in Action: Identification and Monitoring of Bee Species Using ABIS Sustainability in the Information Society. 15th Int. Symp. Informatics for Environmental Protection, p.425-430.
- Batra, S.W.T., 1988. Automatic Image Analysis for Rapid Identification of Africanized Honey Bees. *In: Needham, G.H., Page, R.E., Delfinado-Baker, M., et al.* (Eds.), *Africanized Honey Bees and Bee Mites*. Ellis Horwood, Chichester, UK, p.260-263.
- Comaniciu, D., Meer, P., 2002. Mean shift: a robust approach toward feature space analysis. *IEEE Trans. Pattern Anal. Mach. Intell.*, **24**(5):603-619. [doi:10.1109/34.1000236]
- Gaston, K.J., O'Neill, M.A., 2004. Automated species identification: why not? *Philos. Trans. R. Soc. B: Biol. Sci.*, **359**(1444):655-667. [doi:10.1098/rstb.2003.1442]
- Kingsbury, N., 2001. Complex wavelets for shift invariant analysis and filtering of signals. *Appl. Comput. Harmon. Anal.*, **10**(3):234-253. [doi:10.1006/acha.2000.0343]
- Kokare, M., Biswas, P.K., Chatterji, B.N., 2005. Texture image retrieval using new rotated complex wavelet filters. *IEEE Trans. Syst. Man Cybern.-Part B*, **35**(6):1168-1178. [doi:10.1109/TSMCB.2005.850176]
- MacLeod, N., 2007. *Automated Taxon Identification in Systematics: Theory, Approaches and Applications*. CRC Press, London. [doi:10.1201/9781420008074]
- Mayo, M., Watson, A.T., 2007. Automatic species identification of live moths. *Knowl.-Based Syst.*, **20**(2):195-202. [doi:10.1016/j.knosys.2006.11.012]
- Roth, V., Pogoda, A., Steinhage, V., Schroder, S., 1999. Pattern Recognition Combining Feature- and Pixel-Based Classification within a Real World Application. DAGM Symp. for Pattern Recognition, **21**:120-129.
- Russell, K.N., Do, M.T., Huff, J.C., Platnick, N.I., 2007. Introducing SPIDA-Web: Wavelets, Neural Networks and Internet Accessibility in an Image-Based Automated Identification System. *In: MacLeod, N.* (Ed.), *Automated Object Identification in Systematics: Theory, Approaches, and Applications*. CRC Press, Boca Raton, p.131-152.
- Schroder, S., Wittmann, D., Drescher, W., Roth, V., Steinhage, V., Cremers, A.B., 2002. The New Key to Bees: Automated Identification by Image Analysis of Wings. Proc. Workshop on Conservation and Sustainable Use of Pollinators in Agriculture, p.209-218.
- Shi, J., Malik, J., 2000. Normalized cuts and image segmentation. *IEEE Trans. Pattern Anal. Mach. Intell.*, **22**(8):888-905. [doi:10.1109/34.868688]
- Tofilski, A., 2004. DrawWing, a program for numerical description of insect wings. *J. Insect Sci.*, **4**, Article 17, p.1-5.
- Wang, J.Z., Li, J., Gray, R.M., Wiederhold, G., 2001a. Unsupervised multiresolution segmentation for images with low depth of field. *IEEE Trans. Pattern Anal. Mach. Intell.*, **23**(1):85-91. [doi:10.1109/34.899949]
- Wang, J.Z., Li, J., Wiederhold, G., 2001b. SIMPLiCity: Semantics-sensitive Integrated Matching for Picture Libraries. *IEEE Trans. Pattern Anal. Mach. Intell.*, **23**(9): 947-963. [doi:10.1109/34.955109]
- Watson, A.T., O'Neill, M.A., Kitching, I.J., 2003. Automated identification of live moths (Macrolepidoptera) using the Digital Automated Identification SYstem (DAISY). *System. Biodivers.*, **1**(3):287-300. [doi:10.1017/S1477200003001208]
- Weeks, P.J.D., O'Neill, M.A., Gaston, K.J., Gauld, I.D., 1999. Automating insect identification: exploring the limitations of a prototype system. *J. Appl. Entomol.*, **123**(1):1-8. [doi:10.1046/j.1439-0418.1999.00307.x]
- Yu, D.S., Kokko, E.G., Barron, J.R., Schaalje, G.B., Gowen, B.E., 1992. Identification of ichneumonid wasps using image analysis of wings. *System. Entomol.*, **17**(4):389-395. [doi:10.1111/j.1365-3113.1992.tb00558.x]
- Zhu, L.Q., Zhang, Z., 2010. Auto-Classification of Insect Images Based on Color Histogram and GLCM. 7th Int. Conf. on Fuzzy Systems and Knowledge Discovery, **6**:2589-2593. [doi:10.1109/FSKD.2010.5569848]

Appendix

Table A1 The species and their numbers of specimens used in the experiments

Species	Number of specimens	Species	Number of specimens
<i>Abraxas formosilluminata</i>	4	<i>Herse convolvuli</i>	4
<i>Abraxas suspecta</i>	5	<i>Lethe verma</i>	3
<i>Acherontia styx</i>	3	<i>Loepa anthera</i>	5
<i>Actias selene ningpoana</i>	4	<i>Lymantria viola</i>	4
<i>Agrisius guttivitta</i>	3	<i>Marumba dyras</i>	4
<i>Agrotis ypsilon</i>	5	<i>Marumba gaschkewitschi complacens</i>	5
<i>Agylla prasena</i>	4	<i>Marumba spectabilis</i>	5
<i>Alphaea phasma</i>	4	<i>Miltochrista linga</i>	4
<i>Amathes agalma</i>	3	<i>Miltochrista pulchra</i>	4
<i>Amathes tabida</i>	5	<i>Miltochrista striata</i>	5
<i>Amesia sanguiflua</i>	2	<i>Mustilia falcipennis</i>	4
<i>Ampelophaga rubiginosa</i>	5	<i>Mustilia sphingiformis</i>	3
<i>Anthocharis cardamines</i>	4	<i>Naxa (Ppsilon) seriaria</i>	4
<i>Archips ingentana</i>	3	<i>Nyctemera plagifera</i>	5
<i>Argina argus</i>	5	<i>Obeidia lucifera</i>	5
<i>Arichanna melanaria fraterna</i>	5	<i>Obeidia postmarginata</i>	3
<i>Aroa scytodes</i>	3	<i>Ourapteryx sambucaria</i>	4
<i>Aroa substrigosa</i>	4	<i>Oxyambulyx schauffelbergeri</i>	3
<i>Attacus atlas</i>	4	<i>Pandemis corylana</i>	5
<i>Bireta longivitta</i>	4	<i>Pangrapta trimantesalis</i>	4
<i>Biston melacron</i>	5	<i>Parasa pastoralis</i>	5
<i>Callimorpha plagiata</i>	5	<i>Pernia belluaria sifanica</i>	5
<i>Calospilos sylvata</i>	4	<i>Pericallia galactina</i>	5
<i>Cechenena lineosa</i>	4	<i>Phalera flavescens alticola</i>	5
<i>Cechenena minor</i>	5	<i>Phalera fuscescens</i>	5
<i>Chionaema sanguinea</i>	6	<i>Philosamia cynthia</i>	2
<i>Chrysorithrum amata</i>	4	<i>Phyllosphingia dissimilis sinensis</i>	4
<i>Clanis bilineata tsingtauca</i>	3	<i>Pida postalba</i>	5
<i>Clanis deucalion</i>	4	<i>Pidorus glaucopis</i>	4
<i>Colias erate</i>	4	<i>Problepsis changmei</i>	5
<i>Cretonotos transiens</i>	5	<i>Pseudojana incandescens</i>	4
<i>Cricula andrei</i>	5	<i>Rhagastis yunnanaria</i>	4
<i>Deilemera arctata</i>	5	<i>Rhodogastria astreus</i>	3
<i>Dichromia trigonalis</i>	4	<i>Rhyparioides amurensis</i>	5
<i>Ephesia butleri</i>	4	<i>Sineugraphe disgnosta</i>	5
<i>Ephesia ella</i>	5	<i>Sinna extrema</i>	4
<i>Episteme adulatrix</i>	5	<i>Spilarctia burmanica</i>	5
<i>Erasmia pulchella chinensis</i>	3	<i>Spilarctia comma</i>	5
<i>Eterusia aedeia</i>	5	<i>Spilarctia flavalis</i>	5
<i>Euproctis decussata</i>	4	<i>Spilarctia multivittata assama</i>	5
<i>Euproctis plagiata</i>	4	<i>Spilarctia rubilinea</i>	5
<i>Euproctis staudingeri</i>	4	<i>Spilarctia seriatopunctata</i>	4
<i>Eupterote chinensis</i>	5	<i>Spilosoma menthastri</i>	4
<i>Eupterote diffusa</i>	5	<i>Syntherata loepoides</i>	3
<i>Eupterote geminata</i>	3	<i>Theretra clotho clotho</i>	4
<i>Eupterote lativittata</i>	5	<i>Tigrioides euchana</i>	4
<i>Euxoa oberthuri</i>	4	<i>Toxocampa vulcanica</i>	4
<i>Ganisa pandya</i>	3	<i>Trabala vishnou</i>	4
<i>Heliothis peltigera</i>	5	<i>Uropygia meticulodina</i>	4
<i>Hemerophila emaria</i>	5	<i>Xyleutes mineus</i>	5